SnF_2-Doped Cs_2SnI_6 Ordered Vacancy Double Perovskite for Photovoltaic Applications

*Rubaiya Murshed, Sarah Thornton, Curtis Walkons, Jung Jae Koh, and Shubhra Bansal**

Air-stable p-type SnF_2:Cs_2SnI_6 with a bandgap of 1.6 eV has been demonstrated as a promising material for Pb-free halide perovskite solar cells. Crystalline Cs_2SnI_6 phase is obtained with CsI, SnI_2, and SnF_2 salts in gamma-butyrolactone solvent, but not with dimethyl sulfoxide and *N,N*-dimethylformamide solvents. Cs_2SnI_6 is found to be stable for at least 1000 h at 100 °C when dark annealed in nitrogen atmosphere. In this study, Cs_2SnI_6 has been used in a superstrate n–i–p planar device structure enabled by a spin-coated absorber thickness of ≈2 μm on a chemical bath deposited Zn(O,S) electron transport layer. The best device power conversion efficiency reported here is 5.18% with V_{OC} of 0.81 V, 9.28 mA cm^{-2} J_{SC}, and 68% fill factor. The dark saturation current and diode ideality factor are estimated as 1.5×10^{-3} mA cm^{-2} and 2.18, respectively. The devices exhibit a high V_{OC} deficit and low short-circuit current density due to high bulk and interface recombination. Device efficiency can be expected to increase with improvement in material and interface quality, charge transport, and device engineering.

1. Introduction

Perovskite solar cells (PSCs) have shown remarkable progress in recent years, surpassing the efficiency of conventional thin-film photovoltaic (PV) technologies such as CdTe and CIGS. The recent discoveries in organic–inorganic hybrid PSCs resulting from synergistic optimization of the perovskite absorber layer have generated remarkable development in device efficiency from 3.8% in 2009 to the present state-of-the-art 25.7%.[1–10] Organic–inorganic halide perovskites have also shown 31.3% efficient tandem devices with Si bottom cells.[11] Mixed-halide and mixed-cation systems (e.g., $MAPbI_{1-x}Br_x$; $FA_{0.85}MA_{0.15}PbI_{2.55}Br_{0.45}$; $Cs_{0.1}FA_{0.75}MA_{0.15}PbI_{2.49}Br_{0.51}$) have demonstrated high efficiency, improvement in stability and reduced hysteresis.[12–14] Despite these attractive attributes, some areas need to be addressed on the fundamental materials level, such as materials stability and replacement of Pb with nontoxic and sustainable alternatives.[15–17]

The general formula for halide perovskite is ABX_3, where A is a monovalent organic or alkali metal cation, typically MA^+, Cs^+, Rb^+, etc.; B is divalent p-block metal, e.g., Pb^{2+}, Sn^{2+}, Ge^{2+}, and X is halide anion such as Cl^-, I^- or Br^-.[18,19] Due to its isoelectronic configuration of s^2p^2 similar to Pb and smaller radius (1.35 and 1.49 Å in Sn^{2+} and Pb^{2+}, respectively), Sn is a potential substitute for Pb and can retain original perovskite structure without any significant alteration in lattice parameters.[20,21] However, the oxidation tendency of Sn^{2+} to Sn^{4+} leads to the formation of Sn-cation vacancies that results in metallic conductivity of $CsSnI_3$, $MASnI_3$, $FASnI_3$, and $FAMASnGeI_3$ films.[22–27] Although the film conductivity has been controlled with the addition of SnF_2, $CsSnI_3$ is not stable in atmospheric conditions. Chung et al.[28] have demonstrated 10.2% dye-sensitized solar cells (DSSC) with $CsSnI_3$ electrolytes. Kumar et al.[22] have used 20 mol% SnF_2 additives to modulate the high p-conductivity of $CsSnI_3$ and showed a solid-state perovskite solar cell with a photocurrent density of 22 mA cm^{-2}. The addition of Ge to limit the oxidation of Sn has also shown promise, as Ge^{2+} oxidizes to Ge^{4+}, forming a thin GeO_2 protective layer.[29–31] Ito et al.[32] have fabricated inverted planar devices for $FA_{0.75}MA_{0.25}Sn_{0.95}Ge_{0.05}I_3$ that showed the efficiency of 4.48%, with an increase to 6.90% after 72 h of annealing in N_2 atmosphere. Additives such as ethylenediamine diiodide and guanidinium iodide have been shown to be effective in film crystallization and passivation of recombination centers, demonstrating 8.4% 2D/3D $FASnI_3$ devices.[33,34] Nishimura et al.[35] have reported an efficiency of 13.24% in GeI_2-doped $(FA_{0.9}EA_{0.1})_{0.98}EDA_{0.01}SnI_3$ devices with the highest V_{OC} reaching 0.7 V achieved by surface passivation with the addition of

R. Murshed, S. Thornton, C. Walkons, S. Bansal
Department of Mechanical Engineering
University of Nevada Las Vegas
Las Vegas, NV 89154, USA

J. J. Koh
Department of Chemistry and Biochemistry
University of Nevada Las Vegas
Las Vegas, NV 89154, USA

S. Bansal
School of Mechanical Engineering
School of Materials Engineering
Purdue University
West Lafayette, IN 47907, USA
E-mail: bansal91@purdue.edu

The ORCID identification number(s) for the author(s) of this article can be found under https://doi.org/10.1002/solr.202300165.

DOI: 10.1002/solr.202300165

ethylene diamine diiodide.[36–39] Dimensional modification of Sn-based ABX_3 structures such as low-dimensional Dion–Jacobson Sn(II) or 2D Ruddlesden–Popper (RP) have shown 2.15%, 8.82%, and 14.81% power conversion efficiency (PCE), respectively, for 2D/3D $FASnI_3$.[40–46] While Sn-based PSCs still have room for efficiency and stability enhancements, these developments offer a potential avenue for replacing Pb with a nontoxic and sustainable alternative.

A_2BX_6 is a defect variant of the general perovskite structure ABX_3 where half of the vacant B-cations results in corner-sharing octahedron of anions $[BX_6]^{2-}$ and A-cation occupying the sites between the octahedron in 12-fold coordination.[19] Alteration and substitution of B-cations and/or halogen anions (Cs_2TeI_6,[47] Cs_2PtI_6,[48] Cs_2PbI_6,[49] Cs_2TiBr_6,[50] $Cs_2AgBiBr_6$,[51] $Cs_2AgBiCl_6$,[52] etc.) offer a multitude of features in these double perovskite structures. A_2BX_6 structure offers a broader composition range than the ABX_3 structure optimizing the optoelectronic properties, thermal, and moisture stability.[53–56] Cs_2SnI_6 double perovskite has emerged as a promising light absorber, derived from the cubic 3D structure of $CsSnI_3$, with a 4+ oxidation state of tin and shorter Sn–I bond length (2.85 Å vs 3.11 Å in $CsSnI_3$), making it oxidation resistant and air-stable.[54–58] Intrinsic Cs_2SnI_6 has a direct bandgap of 1.3–1.6 eV,[25,57–60] and is an n-type semiconductor with electron mobility as high as 310 $cm^2 V^{-1} s^{-1}$, ideally suited for theoretical single-junction efficiency of 33%. Interestingly, Cs_2SnI_6 has dual carrier transport characteristics and can be doped p-type with Sn^{2+} exhibiting hole mobility of 42 $cm^2 V^{-1} s^{-1}$.[57] A common concern about vacancy-ordered double perovskites has been that due to low structural dimensionality (isolated $[BX_6]^{2-}$ octahedra), these materials would also exhibit low electronic dimensionality.[61] However, recent results have shown that Cs_2SnI_6 has higher than 0D electronic dimensionality because the close-packed halide framework results in strong overlap between I 5*p* orbitals and Sn and I states between neighboring octahedra. Cs_2SnI_6 has shown to have high dispersion in the conduction band minimum, leading to low electron effective masses of 0.48 m_0 for electrons and 1.32 m_0 for holes.[62] Kapil et al.[60] have reported hole mobilities of 382 $cm^2 V^{-1} s^{-1}$ and hole concentration of 3.65×10^{19} cm^{-3} for solution-processed Cs_2SnI_6 thin-films. Overall, Cs_2SnI_6 is a promising material for use in solar panels because of its high electron and hole mobilities, direct bandgap, and good stability.

Different studies have reported approaches to tune the optoelectronic properties, stability, and device engineering. Qiu et al.[63] have achieved PCE of 0.86% using ZnO nanorod electron transport layer (ETL) and ZnO nanorod/embedded Cs_2SnI_6 light absorber with a device structure of FTO/ZnO/Cs_2SnI_6/P3HT/Ag. Zhang et al.[64] have demonstrated ITO/$CsSnI_3$/Cs_2SnI_6 heterojunction with 1.1% PCE, and these devices retained 90% of the initial performance when exposed to ambient air for 20 h. Air-stable Cs_2SnI_6 films with a bandgap of 1.48 eV and high absorption coefficient have been processed by oxidation of B-γ-$CsSnI_3$ for ≈1% n–i–p planar solar cells.[59] Elemental doping has been reported to tune the optoelectronic properties of Cs_2SnI_6, such as the incorporation of excess Cl or I to improve the stability,[65–67] indium- Cs_2SnI_6 solid solution for enhanced photoluminescence (PL) emission,[68] A-site tailoring with monovalent Rb and Ag,[69] F^- doping to improve film crystallinity in p-type Cs_2SnI_6,[70] and incorporation of Br^- ions to prepare $Cs_2SnI_2Br_4$ films that have achieved PCE of 2.1%.[71] Another approach that has been adopted in several studies is to use the different molar ratios of CsI and SnI_4 to develop this perovskite composition for various optoelectronic applications.[54,60,67–74] Our recently published numerical study suggests the PCE of Cs_2SnI_6 can be increased to >25% by eliminating parasitic losses, optimizing band offsets, reducing mid-gap defect densities, and increasing the absorption coefficient.[53,75] Although significant progress has been made in the efficiency and stability of 2D/3D and 3D Sn(II)-based lead-free perovskite solar cells, limited information exists on Sn(IV)-based Cs_2SnI_6 devices.[12–14,29,35,42,59] Here, we report planar n–i–p ITO/Zn(O,S)/Cs_2SnI_6/carbon/Au devices with best efficiency of 5.18% fabricated by solution processing. Cs_2SnI_6 films were synthesized using a one-step doctor blade method with a 0.4 M solution of CsI and SnI_2 with 20 at% SnF_2 in γ-butyrolactone (GBL) solvent with addition of chlorobenzene antisolvent. Solvents such as dimethyl sulfoxide (DMSO) and *N,N*-dimethylformamide (DMF) were also tested to understand the perovskite phase formation and morphology control. The solution was stirred at 70 °C for 2 h in low humidity conditions. Postdeposition treatment with guanidinium thiocyanate, pyrazine, and ethylene diamine followed by 100 °C anneal for up to an hour in vacuum, has also been explored for perovskite film formation and defect passivation.[76–83] For device fabrication, the precursor solution was spin-coated on ITO glass following chemical bath deposition of Zn(O,S). The device stack was completed with EDA postdeposition treatment, carbon paste, and evaporated Au.

2. Results and Discussion

2.1. Solvent Effect on Cs_2SnI_6 Phase Formation

Solvent selection plays a key role in the formation of halide perovskites, crystal quality, and pinhole-free deposition using doctor blade or spin-coating methods. Hao et al. have shown the formation of pinhole-free $CH_3NH_3SnI_3$ perovskite films with DMSO solvent via the formation of SnI_2·3DMSO intermediate phase.[84] However, Pascual et al. have reported that DMSO oxidizes Sn(II) to Sn(IV) limiting the performance of Sn-halide perovskites at 10%–14%.[85] In our study of ambient deposition, CsI, SnI_2, and SnF_2 in GBL solvent results in the formation of a dark-colored precursor solution and shows a narrow direct bandgap of 1.3–1.5 eV. DMF- and DMSO-based precursors result in films with 2 and 2.5 eV bandgap, respectively, as shown in **Figure 1**a. The X-ray diffraction (XRD) patterns (Figure 1b) show that these dark films with GBL are primarily crystalline Cs_2SnI_6 phase with small amounts of unreacted CsI, which can be eliminated with the use of additives such as pyrazine or ethylene diamine. DMSO solvent results in the formation of a yellow precursor solution resulting in films primarily containing wide-bandgap CsI as detected by the (101), (200), and (400) peaks in the XRD pattern. DMSO is a dipolar aprotic solvent that has been shown to form an intermediate such as PbI_2·DMSO or SnI_2·3DMSO phase or oxidation of iodide to iodine;[83–85] limiting the formation of Sn-perovskite. DMF-based precursor solution is a dark reddish-black color resulting in films with significantly suppressed CsI peak as observed in XRD. DMF-based films are more

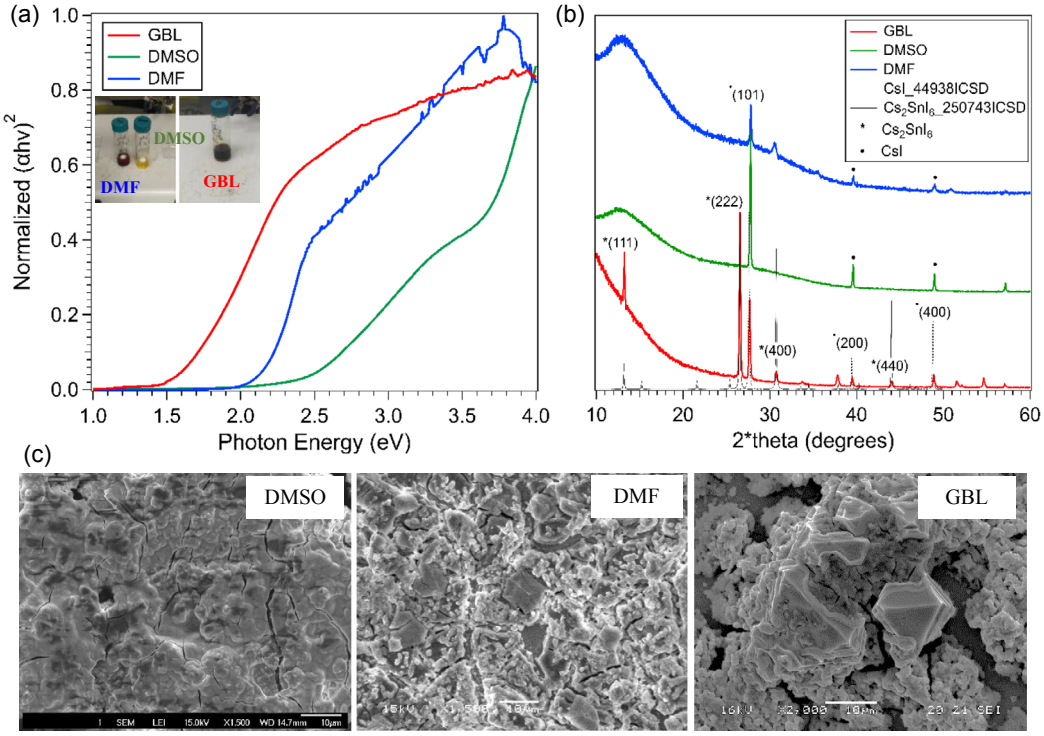

Figure 1. a) Tauc plot showing bandgap, b) XRD pattern, c) Film morphology, of Cs_2SnI_6 perovskite with different solvents, namely gamma-butyrolactone (GBL); *N,N*-dimethylformamide (DMF); dimethyl sulfoxide (DMSO).

amorphous with lower intensity for CsI (101) peak and small crystallite size, resulting in a wide bandgap of 2 eV. Films processed with both DMF and DMSO solvents do not show the (222) Cs_2SnI_6 peak, suggesting incomplete formation of perovskite phase. Further, the small crystallite size or higher fraction of amorphous phase can result in wider bandgap films.[86] Both DMF and DMSO solvent-based films also show higher background signal at low 2*theta values in XRD indicating poor crystallinity as confirmed by scanning electron microscopy. Figure 1c shows the scanning electron microscopy (SEM) images depicting the morphology of films deposited using DMSO, DMF, and GBL solvents, respectively. DMF- and DMSO-based films have poor morphology and crystallinity, whereas GBL results in large Cs_2SnI_6 crystallites, with high density of pinholes. Tin halide is a Lewis acid and the three solvents GBL, DMF, and DMSO are Lewis bases with donor numbers (D_N) of 18, 26.6, and 29.8 kcal mol^{-1}, respectively. The high D_N of DMF and DMSO retards perovskite crystal growth forming glass-like films with wider bandgap. The wide bandgap of the films and absence of Cs_2SnI_6 characteristic peaks in XRD suggest that the formation of Cs_2SnI_6 is inhibited by the solvent co-ordination to the metal precursor for DMF and DMSO. To determine the mechanism of formation of intermediate phase we conducted Fourier transform infrared (FTIR) spectroscopy.

Figure 2a shows the FTIR spectra for GBL solvent and precursor solution with the addition of $CsI + SnI_2 + SnF_2$ solutes, showing a shift in the peaks to lower wavenumber and an increase in the intensity of C═O bond indicating intermediate phase formation with this functional group. In metal halide perovskite solutions, atoms, ions, and solvent molecules coordinate, forming specific solvate intermediate phases. It has been shown that strong coordination interactions can be formed when the lone electron pairs in the functional groups (–NH and –CO) are delocalized to the 5*p* empty orbitals of Sn^{2+} ($4d^{10}5s^2$) in $CsSnI_3$. Subsequently, with annealing, the B-γ-$CsSnI_3$ evolves into Cs_2SnI_6, creating discrete molecular $[SnI_6]^{2-}$ octahedra with Sn^{4+} oxidation state. FTIR spectrum of DMF-based precursor solution shows stretching of CH_3–N–CH_3 bond as shown by an increase in the intensity of the 553 cm^{-1} wavenumber peak (Figure 2b), which is nonexistent in the solvent spectrum. The peak represents intermediate phase formation with DMF limiting perovskite formation. DMSO-based precursor solution shows the additional peak at 552 cm^{-1} as well as stretching of sulfoxide bonds indicating their role in limiting the formation of perovskite phase as shown in Figure 2c. A comparison of the three solvents shows GBL is best for precipitation of Cs_2SnI_6 crystallites, however, the film quality is powder-like with discrete crystals. The use of chlorobenzene antisolvent and additives assists film crystallization and passivation as discussed in the following sections.

Figure 3 shows that addition of SnF_2, GuaSCN, EDA, as well as pyrazine assists with the crystallization of Cs_2SnI_6. Films with 20 at% SnF_2 added to $CsI + SnI_2$ in GBL show a coexistence of amorphous and crystalline region and not much improvement in film morphology, as shown in Figure 3a. Figure 3b shows improved film crystallization with the use of SnF_2 and GuaSCN additives, however, many pinholes are observed due to rapid crystal growth before nucleation is complete. SEM images in Figure 3c,d show uniform polycrystalline films with

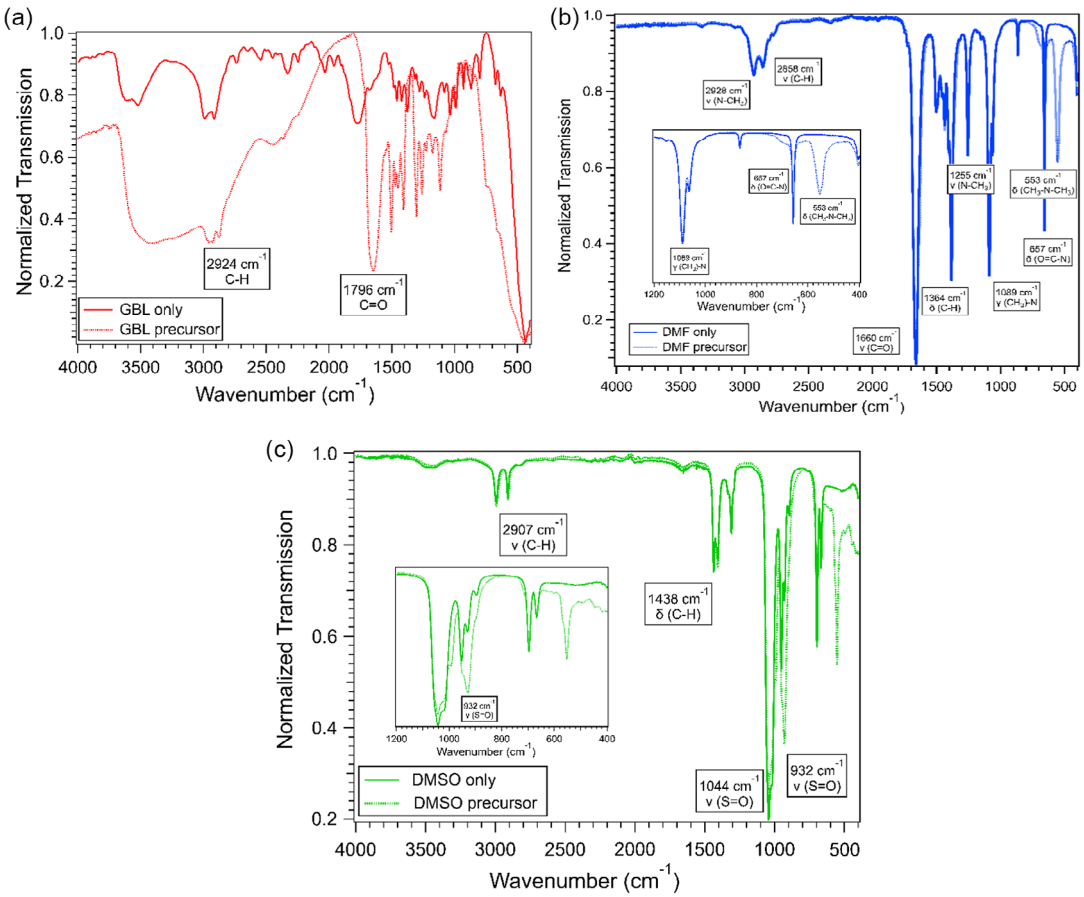

Figure 2. Fourier transform infrared (FTIR) spectra for solvent and precursor solution (solvent + CsI + SnI_2 + SnF_2 for a) gamma-butyrolactone (GBL); b) *N*,*N*-dimethylformamide (DMF); c) Dimethyl sulfoxide (DMSO). Insets for (b) and (c) show the wavenumber range of 1200 to 400 cm^{-1} to zoom on the peak changes.

EDA without any pinholes. The use of diamines like EDA and pyrazine as a postdeposition treatment has multiple advantages including defect passivation, film morphology, and improvement in V_{OC}.[87,88] Previous studies suggest the addition of EDA balances the rate between nucleation and crystal growth, where it slows down crystal growth to achieve uniform nucleation and form compact pinhole-free perovskite films,[22] as observed here. Song et al.[89] and Lee et al.[82] have previously highlighted the critical role of the diamine group in piperazine and pyrazine, respectively, to assist the formation of perovskite films with improved crystallinity and coverage. EDA and pyrazine, being strong Lewis bases are also effective mediators for excess SnF_2 resulting in enhanced crystallinity and F^- doping.[90] Diamine-based additives can accept lone pairs from SnI_2 and SnF_2 forming complexes and thereby effectively control the Sn vacancies and prevent phase segregation due to the presence of excess SnF_2 in the precursor solution.[82] The passivation effect of guanidinium-based salt such as guanidinium thiocyanate (GuaSCN) has also been reported as a potential approach to positively affect the nucleation process, initiate grain structure optimization, suppress the formation of Sn-vacancy, and improve photovoltaic performance.[76–80] Pyrazine postdeposition treatment has shown to passivate the surface and grain-boundary defects in Pb-based PSCs, enhancing device efficiency from 19.14% to 20.58%.[81] As shown in Figure 3c, Cs_2SnI_6 films with EDA postdeposition treatment are polycrystalline with thickness range of 1.67–2.16 µm.

Figure 4a shows the XRD patterns of perovskite films deposited with and without additives to understand the phase transformations. No significant change in lattice parameters and perovskite crystal structure resulted from the addition of SnF_2, suggesting F^- does not substitute I^- because of its smaller ionic radii of 1.33 Å compared to 2.2 Å of the latter one, similar to what has been observed in previous studies.[26,90–92] A clear reduction in the intensity of CsI (101) and CsI (200) peaks at $2\theta = 27.8°$ and 39.5°, and enhancement in the intensity of Cs_2SnI_6 (222) peak at $2\theta = 26.5°$ has been observed with the addition of SnF_2. XRD spectra suggest the formation of crystalline Cs_2SnI_6 films with pyrazine and EDA treatments without CsI impurities and preferred orientation on the (222) crystal plane, indicating fewer defects in these films. The addition of GuaSCN did not result in any significant changes in the crystal planes, and the relative intensity ratio of the Cs_2SnI_6 (222) and the CsI (101) plane was found to be similar to the SnF_2-added films, suggesting a small amount of GA does not affect the perovskite structure.[76,79] The peak broadening of the XRD pattern is inversely correlated

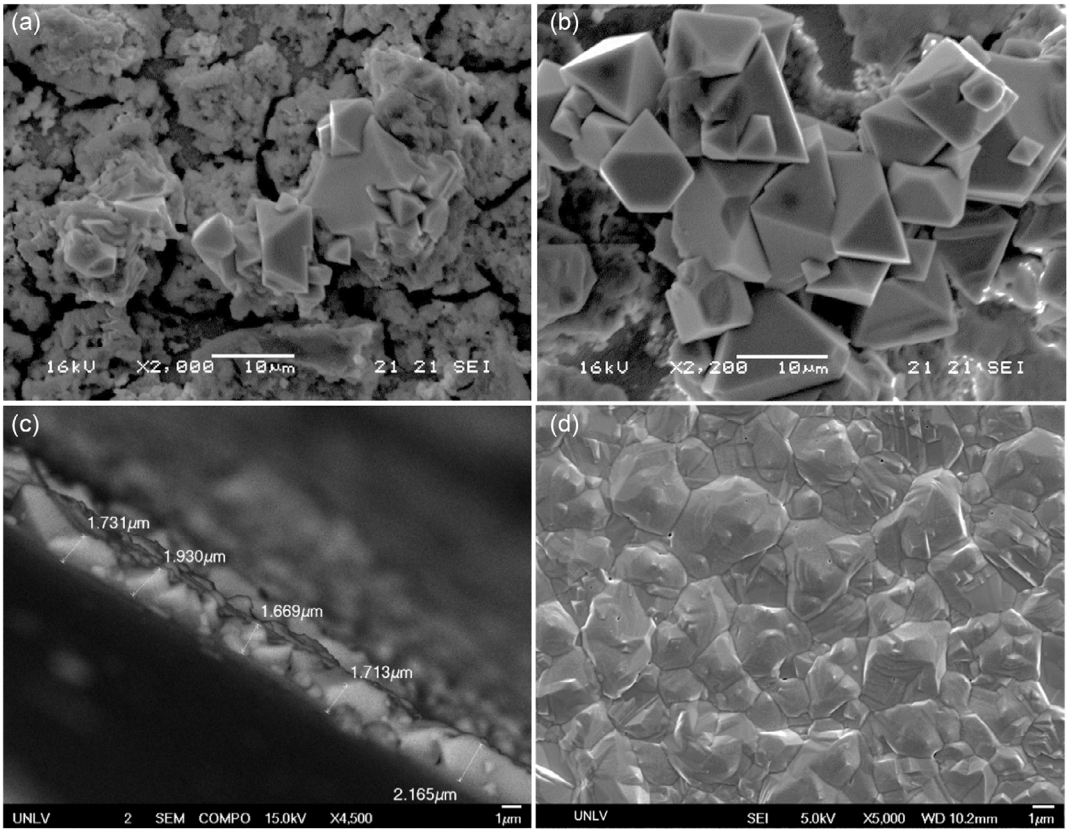

Figure 3. Film morphology of Cs_2SnI_6 perovskite with different additives, such as, a) SnF_2, b) GuaSCN + SnF_2, c) EDA + SnF_2 (cross-sectional thickness on cleaved sample), d) EDA + SnF_2.

with crystallite size. Perovskite films with large crystallite sizes can have reduced grain boundaries and reduced carrier recombination, which increases carrier mobility.[93] The peak broadening in our films with no additives is reduced to some extent with the addition of SnF_2, while a further reduction in peak broadening is observed with the additional additives, especially with pyrazine and EDA, which is in good alignment with the compact microstructure of EDA-induced films shown in Figure 3d. Due to the good binding affinity to SnF_2, pyrazine, and EDA facilitate Sn-vacancy reduction and hinder phase segregation that comes from the presence of excess SnF_2 in the precursor solution, which is in good alignment with the reflection of phase pure Cs_2SnI_6 without any CsI peak as observed in the XRD analysis.[89] Cs_2SnI_6 has been reported to have a direct bandgap between 1.25 and 1.62 eV, here we estimate the bandgaps using UV–vis-NIR transmittance spectrum and the plot of $(\alpha h\vartheta)^2$ versus photon energy, as shown in Figure 4b. With effective F-doping using amine-based additives strong electrostatic attraction, and hence an increase in the energy gap is expected. Films without SnF_2 exhibit a primary direct bandgap of 1.2–1.3 eV with a secondary wider bandgap over 2 eV. The primary bandgap widens to 1.5–1.6 eV with the use of SnF_2 and additives such as pyrazine and ethylene-diamine, as also confirmed by photoluminescence (PL) emission peak at 1.61 eV (Figure 4c). To determine the phase stability of Cs_2SnI_6 films with SnF_2 and EDA, we annealed the films at 100 °C for 1000 h in nitrogen atmosphere. XRD patterns shown in Figure 4d, point toward the intrinsic stability of Cs_2SnI_6 as has also been previously demonstrated by Saparov et al.[58] Here, we observe that EDA served a dual function, first, it helps to incorporate SnF_2 in the films and passivation of defects, surfaces, and grain boundaries, as shown in Figure 4e. As no peak shift is observed in diffraction patterns with the incorporation of SnF_2, we infer that F^- does not replace I^- in bulk, however, can occupy I-vacancies at grain boundaries.

Incorporation of these diamine compounds passivated the defects in the bulk, surface, and grain boundaries resulting in a reduced recombination rate as measured by enhanced minority carrier diffusion lifetime as shown in **Figure 5**a. The use of GuaSCN and EDA improves the film crystallinity and reduces CsI residual phase thereby decreasing charge carrier recombination and increasing the carrier lifetime. With GuaSCN additive the minority carrier lifetime shows a marginal increase to 4.3 ns. The minority carrier lifetime for films with only SnF_2 is measured as 3.74 ns that improves to 6.23 and 6.06 ns with pyrazine and EDA additives respectively. Carrier density and mobility have been measured using Hall measurements on thin film samples with and without SnF_2 and EDA, as shown in Figure 5b,c. All the films processed with SnF_2 have p-type semiconductor properties, showing an increase in carrier density and mobility over samples without SnF_2. Undoped Cs_2SnI_6 shows an average carrier density of $\approx 10^{14}\,cm^{-3}$ and mobility of $7\,cm^2\,V^{-1}\,s^{-1}$, whereas with SnF_2 doping, an increase to $6 \times 10^{14}\,cm^{-3}$ and $18\,cm^2\,V^{-1}\,s^{-1}$

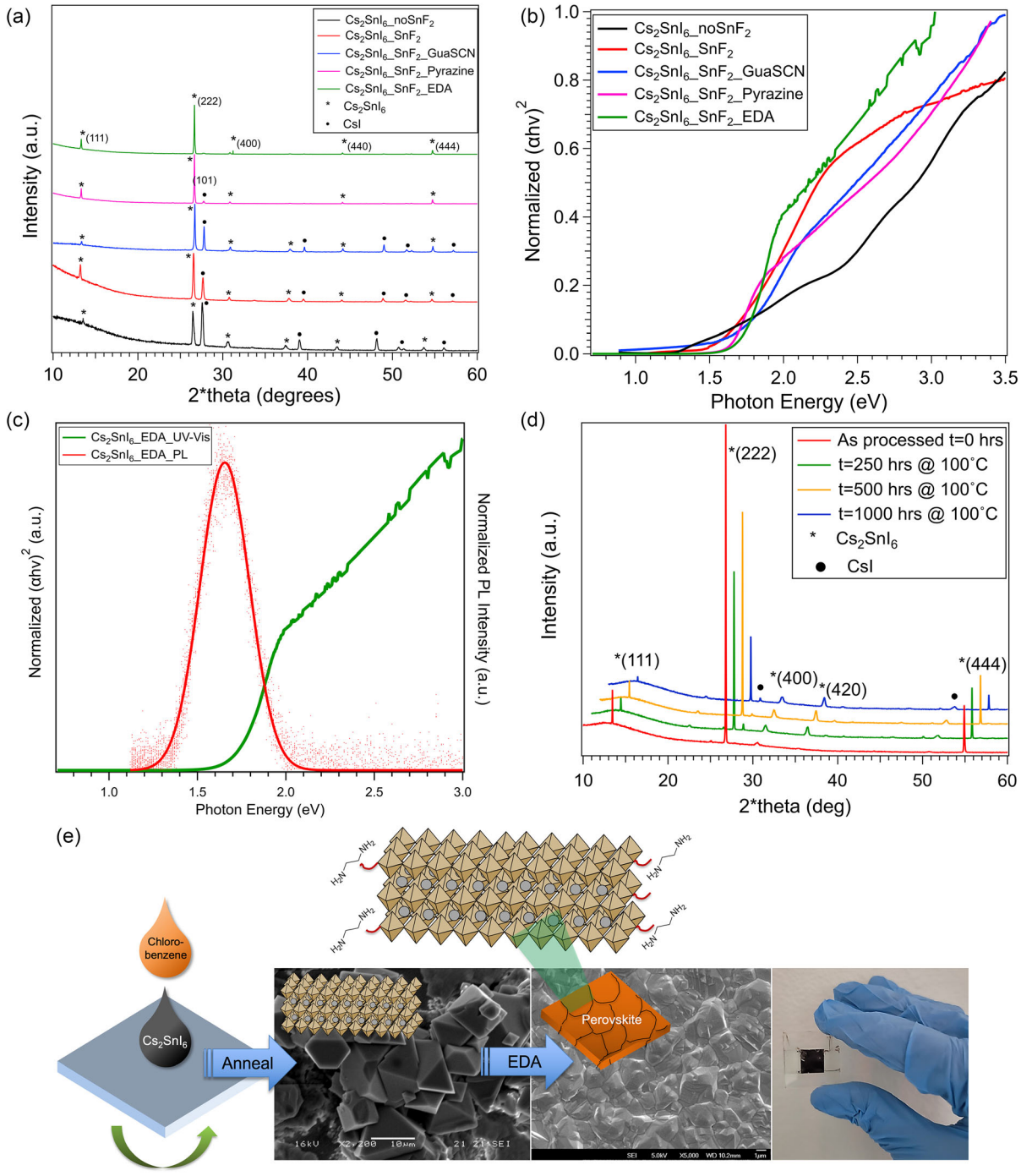

Figure 4. a) XRD pattern Cs_2SnI_6 films with additives SnF_2, GuaSCN + SnF_2, Pyrazine + SnF_2, ethylene diamine (EDA) + SnF_2, b) Tauc plot showing bandgap of Cs_2SnI_6 film with additives SnF_2, GuaSCN + SnF_2, pyrazine + SnF_2, ethylene diamine (EDA) + SnF_2. c) Tauc plot and PL emission for EDA-treated films processed with CsI + SnI_2 + SnF_2 in GBL. d) XRD pattern for annealed Cs_2SnI_6 films. e) Schematic depicting the perovskite formation using CsI, SnI_2, and SnF_2 in GBL solvent with guanidium thiocyanate, chlorobenzene antisolvent, and ethylene diamine (EDA) postdeposition treatment.

is observed. With EDA treatment, the carrier density increases from $5.5 \times 10^{14}\,cm^{-3}$ to $6.9 \times 10^{14}\,cm^{-3}$, and hole mobility increases in marginal. An increase in carrier lifetime supports the passivation effect of EDA and an increase in carrier density is likely due to better incorporation of F^- ions from SnF_2.

To evaluate the device performance, we synthesized ITO/Zn(O,S)/SnF_2-Cs_2SnI_6/carbon/Au devices with EDA postdeposition treatment, as shown in **Figure 6**a. Figure 6b,c shows the dark and light current–voltage (J–V) performance of champion cells and external quantum efficiency (EQE) curves, respectively.

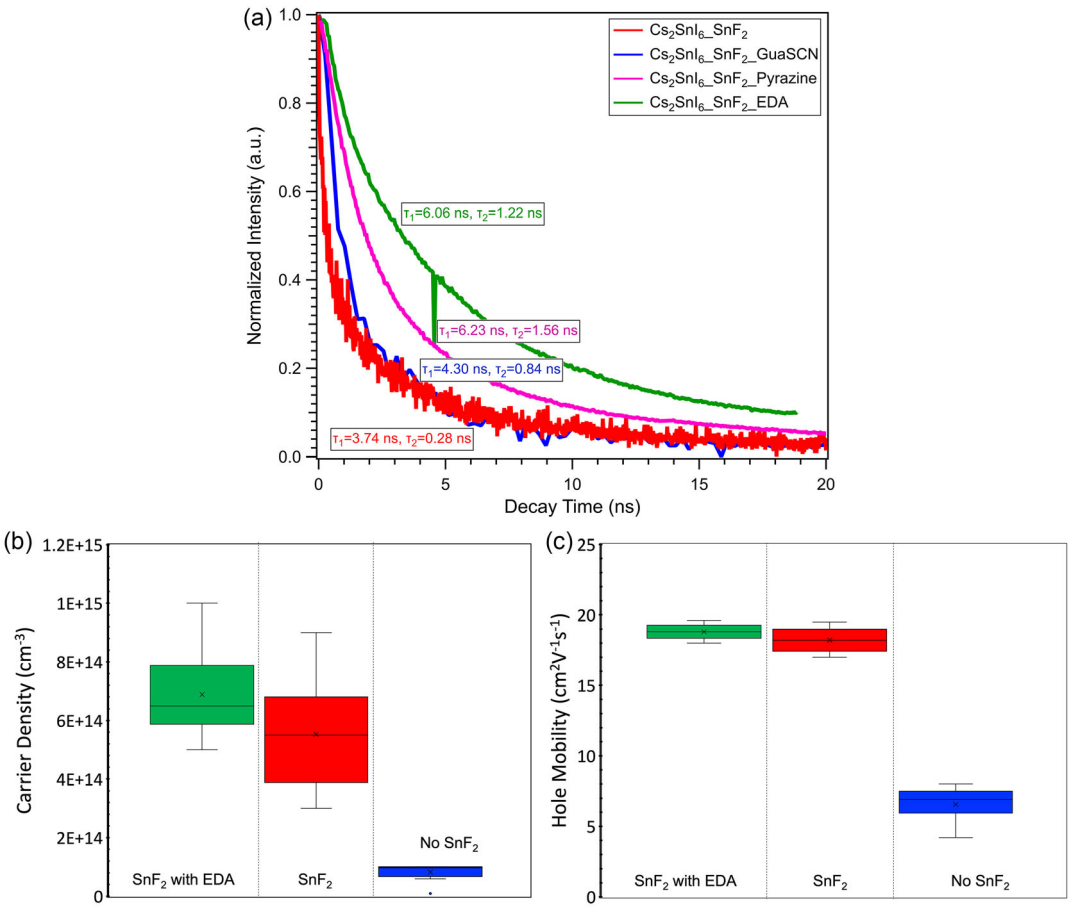

Figure 5. a) Minority carrier lifetime in SnF_2-doped Cs_2SnI_6 films with additives GuaSCN, pyrazine, EDA; b) carrier density of pristine (no SnF_2) and additive-assisted Cs_2SnI_6 films with SnF_2 and EDA, c) hole mobility of pristine (no SnF_2) and additive-assisted Cs_2SnI_6 films with SnF_2 and EDA.

The best device with SnF_2 only (no EDA) showed an efficiency of 2.39% with a J_{SC} of 7.55 mA cm^{-2}, V_{OC} of 0.625 V, and a fill factor (FF) of 50.79%. With the addition of EDA, efficiency increased to 5.18% with a J_{SC} of 9.28 mA cm^{-2}, V_{OC} of 0.81 V, and a fill-factor (FF) of 68.89%. The integrated quantum efficiency is calculated as 5.8 mA cm^{-2} for devices without EDA and 9.3 mA cm^{-2} for devices with EDA postdeposition treatment. It is noted that devices without EDA treatment exhibit voltage-dependent current collection as evident from the J–V data resulting in the discrepancy between light-generated current and integrated quantum efficiency (IQE). The increase in device performance with the addition of EDA is attributed primarily to increased V_{OC} and FF due to better collection efficiency, as indicated by enhanced long-wavelength QE and minority carrier lifetime. Next, we evaluated the dark saturation current density (J_0) and ideality factor (A) for the devices to understand the effect of EDA + SnF_2 treatment on the recombination and parasitic losses. J–V behavior of planar thin-film devices can be described by a single exponential diode equation

$$J = J_0 \exp\left[\frac{q}{AkT}(V - RJ)\right] + GV - J_L \quad (1)$$

Where q is the electron charge, k is Boltzmann constant, T is the temperature in Kelvin, R is series resistance, G is shunt conductance, and J_L is light-generated current. The derivative $\frac{dV}{d(J-GV)}$ against $(J - GV)^{-1}$ is plotted for constant $J_L = J_{SC}$, and the slope should be $\frac{AkT}{q}$, from which A can be calculated. The diode ideality factor, A, is estimated as 2.45 without and 2.18 with the use of EDA, and J_0 is 6.5×10^{-3} and 1.5×10^{-3} mA cm^{-2}, respectively, listed in **Table 1**. The diode ideality factor in the range 1 to 2 represents Shockley–Reed Hall nonradiative recombination of carriers. The A-value for these Cs_2SnI_6 planar devices is greater than 2 suggesting additional mechanisms such as Auger and/or interface recombination. The decrease in J_0, increase in FF, and carrier lifetime all indicate passivation effect of EDA leading to improvement in device efficiency. Figure 6d shows the box plot of device parameters for 10 devices of each type with and without EDA. The average efficiency improves from 1.52% to 4.54% with EDA with an increase of J_{SC}, V_{OC}, and FF. The use of EDA marginally improves the current collection and V_{OC}. However, further improvements such as optimized absorber thickness, improved carrier density, and lifetime are needed to address the V_{OC}-deficit, and low short-circuit current density. Figure 6e shows the SEM micrograph for Cs_2SnI_6 deposited on Zn(O,S) layer depicting the film nonuniformity.

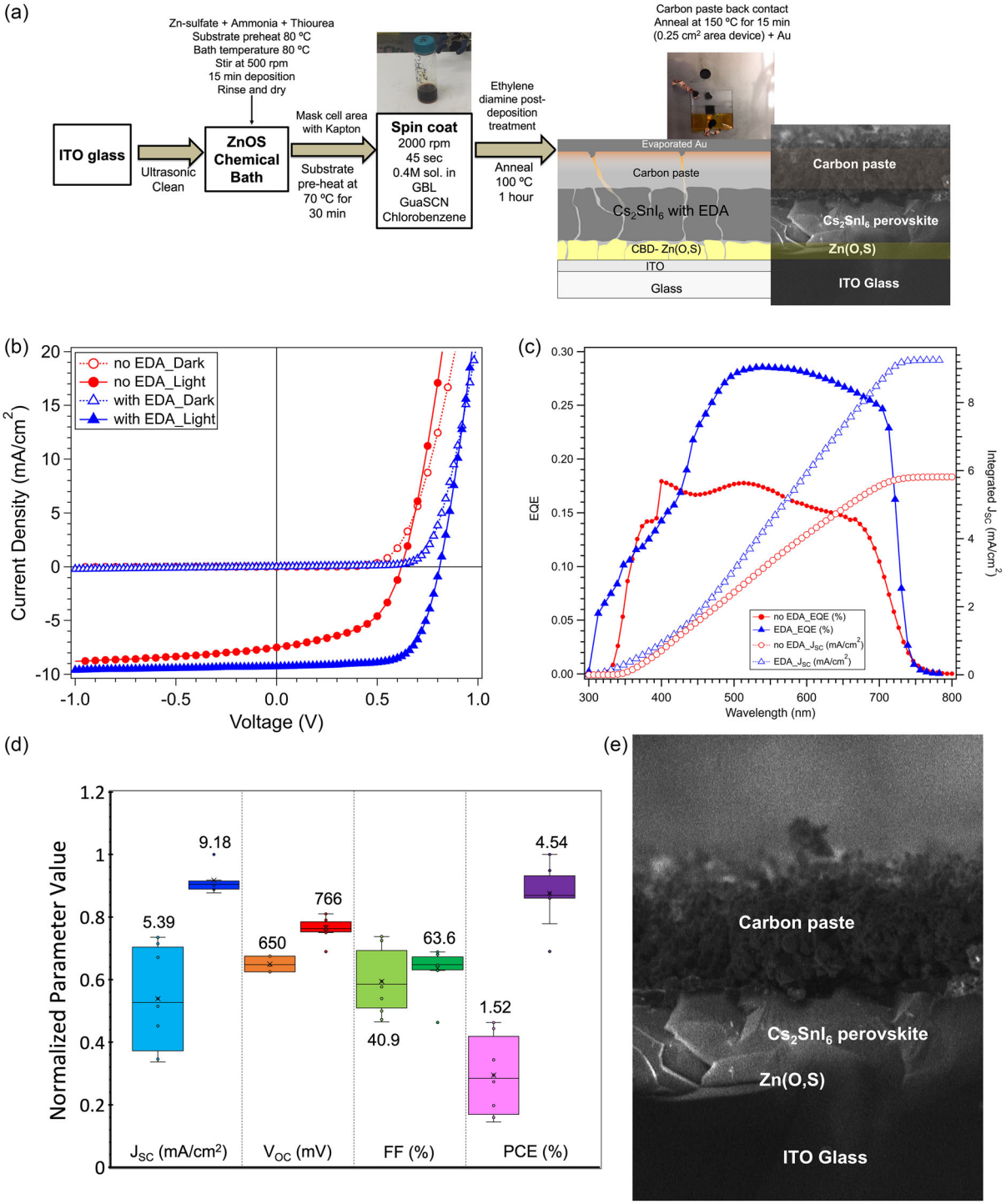

Figure 6. a) Process flow for device fabrication; b) dark and light current density–voltage (J–V) performance of champion cells with and without EDA postdeposition treatment, c) external quantum efficiency (EQE) and integrated J_{SC} curves for Cs_2SnI_6 devices with and without EDA postdeposition treatment d) box-plot for normalized device parameters showing the effect of EDA with 10 devices of each type, average values listed, and e) cross-section SEM micrograph of ITO/Zn(O,S)/Cs_2SnI_6/carbon device stack.

Table 1. Device performance parameters for SnF_2-doped Cs_2SnI_6 perovskite champion cell with and without EDA.

Device type	PCE [%]	V_{OC} [V]	J_{SC} [mA cm^{-2}]	FF [%]	A	J_0 [mA cm^{-2}]
No EDA	2.39	0.625	7.55	50.79	2.45	6.5×10^{-3}
With EDA	5.18	0.81	9.28	68.89	2.18	1.5×10^{-3}

3. Conclusion

In this report, we have demonstrated the formation of crystalline Cs_2SnI_6 phase with a solvent of GBL, chlorobenzene antisolvent and SnF_2, guanidinium thiocyanate, and ethylene diamine additives in a superstrate n–i–p planar device structure. GBL as a solvent helps in the formation of low bandgap (1.3–1.5 eV) Cs_2SnI_6 perovskite phase with a small amount of unreacted CsI, which has been reduced with additives. The strong interaction between the Lewis base EDA and the Sn species improves the morphology, passivates the grain boundaries, and results in a larger grain size and pinhole-free surface with a direct bandgap of 1.6 eV. SnF_2-doped crystalline Cs_2SnI_6 films with diamine-based additives show significantly suppressed CsI and Cs_2SnI_6 preferred orientation along the (222) crystal plane and have a minority carrier lifetime of over 6 ns, which is almost twice the lifetime in films with only SnF_2. The champion cell having an efficiency of 5.18% with EDA is primarily attributed to an increase in the V_{OC} and FF, which confirms a better collection efficiency with EDA as indicated by enhanced long-wavelength QE and minority carrier lifetime. The hole mobility of Cs_2SnI_6 films is measured to be around 18 cm^2 V^{-1} s^{-1} and carrier concentration of 6×10^{14} cm^{-3} indicating room for improvement in the film quality. These devices are dominated by high interface and bulk recombination rates as indicated by the diode quality factor of 2.18 and dark saturation current of 1.5×10^{-3} mA cm^{-2}. Future work will include improving film quality and alternate electron and hole transport layers for reducing interface recombination and enhancing bulk and interface passivation. The results presented are promising toward a Pb-free perovskite thin-film devices with a bandgap well suited for a top cell in tandem with technologies such as crystalline Si or Cu(In,Ga)Se_2 solar cells.

4. Fabrication and Characterization Methods

Cs_2SnI_6 films were synthesized on ITO glass using a 0.4 M equimolar solution of CsI (CAS No. 7789-17-5), SnI_2 (CAS No. 10294-70-9) in a solvent mixture of GBL (CAS No. 96-48-0), chlorobenzene (CAS No. 108-90-7), and 20 at% SnF_2 (CAS No. 7783-47-3). 0.5196 gm of CsI and 0.745 gm of SnI_2 in 5 mL of solvent were stirred at 70 °C for 2 h in low-humidity conditions resulting in a blackish-brown solution. A 10-second spray postdeposition treatment of guanidinium thiocyanate (GuaSCN, CAS No. 593-84-0), pyrazine (CAS No. 290-37-9), or ethylene diamine (EDA, Sigma Aldrich CAS No. 391085) were used for enhanced film morphology and passivation. The glass substrates were preheated at 70 °C for 30 min, and after doctor blade or spin coating, the films were annealed at 100 °C in a vacuum oven for 30 min to an hour. For device processing Zn(O,S) was deposited using chemical bath deposition using zinc sulfate (CAS No. 7446-20-0), thiourea (CAS No. 62-56-6), and ammonium hydroxide (CAS No. 1336-21-6) at 80 °C, while stirring at 500 rpm. 11.952 gm of $ZnSO_4$ and 9.13 gm of thiourea were mixed with 127 mL of NH_4OH and 72 mL of DI water and HCl were used to maintain a solution pH of 11. The substrates were then cleaned with 2.5% ammonium hydroxide solution and water, followed by air drying. The sunny side of the glass was cleaned with dilute HCl, and then Zn(O,S) substrates were preheated at 70 °C, followed by Cs_2SnI_6 deposition. 100 µL of 0.4 M precursor solution of CsI, SnI_2, 20 at% SnF_2 in GBL solvent was spin-coated for 45 s at 2000 rpm with chlorobenzene dispensed at 20 s. The devices were completed by application of carbon paste ElectroDAG 440B from Acheson[94] followed by annealing at 150 °C for 15 min and evaporated Au for an active device area of 5 mm × 5 mm, as shown in Figure 6a. About 100 films and 10 functional devices have been consistently fabricated using this process. It is noted that SnI_4 did not result in the Cs_2SnI_6 phase. Further, this phase did not form without the use of SnF_2. To improve the wettability and coverage on glass or Zn(O, S), 50 µL of chlorobenzene was dispensed at about 20 s into the spin coating cycle. Current–voltage characteristics were measured using an ABET solar simulator calibrated to 1 sun and Keithley 2400 source meter with a 10 mV step size. The EQE spectra were obtained using the QE XL+ tool from PV Measurements Inc. consisting of a xenon lamp, a monochromator, a lock-in amplifier, and calibrated Si and Ge photodetectors. For quantum efficiency, the integrated quantum efficiency (IQE) or integrated J_{SC} was solved via Equation (2)

$$\mathrm{IQE} = \int_{\lambda_{\mathrm{start}}}^{1200\mathrm{nm}} \frac{q\lambda}{hc}\left(\frac{\mathrm{QE}}{100}\right) E_{0,\mathrm{AM1.5}}(\lambda)\,d\lambda \tag{2}$$

where $E_{0,AM1.5}$ is the AM1.5G spectral irradiance, QE is the quantum efficiency, and q is the elementary unit charge. Time-resolved photoluminescence (TRPL) measurements were conducted at Molecular Foundry using a setup built around a Nikon Eclipse Ti-U microscope with 0.3 NA objective. For one-photon excitation, a 405 nm nanosecond pulsed laser system (Thorlabs NPL41B, 6 ns pulse width, 1 MHz repetition rate) was used and photoluminescence was filtered with 540 and 532 nm long-pass filters. X-ray diffraction (XRD) measurements were conducted on a Bruker diffractometer under ambient conditions using Cu Kα radiation. Mercury was used to create crystal structure (ICSD 250743) and PDF-4 was used for XRD data analysis and phase identification. Optical transmittance and reflectance measurements were performed using Shimadzu UV-2600 spectrophotometer and light soaking experiments were conducted in ATLAS XXL+ solar simulator. Carrier mobility and conductivity were measured using a van der Pauw test structure in Ecopia HMS5500 Hall effect measurement method.

Acknowledgements

This research has been funded by the University of Nevada Las Vegas Top Tier Doctoral Graduate Research Assistantship (TTDGRA), NextEra Energy Research Fellowship and partly by UNLV's National Science Foundation's Innovation Corps (NSF-iCORPS) and NSF CAREER award number 2046944.

Conflict of Interest

The authors declare no conflict of interest.

Data Availability Statement

The data that support the findings of this study are available from the corresponding author upon reasonable request.

Keywords

Cs_2SnI_6, ethylene diamine, gamma-butyrolactone, lead-free, perovskite solar cells, planar device, SnF_2

Received: March 2, 2023
Revised: June 14, 2023
Published online: August 6, 2023

[1] M. Green, E. Dunlop, J. Hohl-Ebinger, M. Yoshita, N. Kopidakis, X. Hao, *Prog. Photovoltaics: Res. Appl.* **2021**, *29*, 3.
[2] W. S. Yang, J. H. Noh, N. J. Jeon, Y. C. Kim, S. Ryu, J. Seo, S. I. Seok, *Science* **2015**, *348*, 1234.
[3] N. J. Jeon, J. H. Noh, W. S. Yang, Y. C. Kim, S. Ryu, J. Seo, S. I. Seok, *Nature* **2015**, *517*, 476.
[4] H. Zhou, Q. Chen, G. Li, S. Luo, T.-B. Song, H.-S. Duan, Z. Hong, J. You, Y. Liu, Y. Yang, *Science* **2014**, *345*, 542.
[5] A. Kojima, K. Teshima, Y. Shirai, T. Miyasaka, *J. Am. Chem. Soc.* **2009**, *131*, 6050.
[6] W. S. Yang, B.-W. Park, E. H. Jung, N. J. Jeon, Y. C. Kim, D. U. Lee, S. S. Shin, J. Seo, E. K. Kim, J. H. Noh, S. I. Seok, *Science* **2017**, *356*, 1376.
[7] E. H. Jung, N. J. Jeon, E. Y. Park, C. S. Moon, T. J. Shin, T.-Y. Yang, J. H. Noh, J. Seo, *Nature* **2019**, *567*, 511.
[8] Q. Jiang, Y. Zhao, X. Zhang, X. Yang, Y. Chen, Z. Chu, Q. Ye, X. Li, Z. Yin, J. You, *Nat. Photonics* **2019**, *13*, 460.
[9] M. Kim, G.-H. Kim, T. K. Lee, I. W. Choi, H. W. Choi, Y. Jo, Y. J. Yoon, J. W. Kim, J. Lee, D. Huh, H. Lee, S. K. Kwak, J. Y. Kim, D. S. Kim, *Joule* **2019**, *3*, 2179.
[10] J. Burschka, N. Pellet, S.-J. Moon, R. Humphry-Baker, P. Gao, M. K. Nazeeruddin, M. Grätzel, *Nature* **2013**, *499*, 316.
[11] Best Research-Cell Efficiency Chart | Photovoltaic Research | NREL, https://www.nrel.gov/pv/cell-efficiency.html (accessed: January 2023).
[12] L. K. Ono, E. J. Juarez-Perez, Y. Qi, *ACS Appl. Mater. Interfaces* **2017**, *9*, 30197.
[13] B.-B. Yu, M. Liao, Y. Zhu, X. Zhang, Z. Du, Z. Jin, D. Liu, Y. Wang, T. Gatti, O. Ageev, Z. He, *Adv. Funct. Mater.* **2020**, *30*, 2002230.
[14] W. Ke, C. C. Stoumpos, M. Zhu, L. Mao, I. Spanopoulos, J. Liu, O. Y. Kontsevoi, M. Chen, D. Sarma, Y. Zhang, M. R. Wasielewski, M. G. Kanatzidis, *Sci. Adv.* **2017**, *3*, e1701293.
[15] L. Meng, J. You, Y. Yang, *Nat. Commun.* **2018**, *9*, 5265.
[16] M. Ke, Q. Song, *Chem. Commun.* **2017**, *53*, 2222.
[17] Q. Xu, D. Yang, J. Lv, Y.-Y. Sun, L. Zhang, *Small Methods* **2018**, *2*, 1700316.
[18] L. Liang, P. Gao, *Adv. Sci.* **2018**, *5*, 1700331.
[19] P. Gao, M. Grätzel, M. K. Nazeeruddin, *Energy Environ. Sci.* **2014**, *7*, 2448.
[20] T. Leijtens, R. Prasanna, A. Gold-Parker, M. F. Toney, M. D. Mcgehee, *ACS Energy Lett.* **2017**, *2*, 2159.
[21] N. K. Noel, S. D. Stranks, A. Abate, C. Wehrenfennig, S. Guarnera, A.-A. Haghighirad, A. Sadhanala, G. E. Eperon, S. K. Pathak, M. B. Johnston, A. Petrozza, L. M. Herz, H. J. Snaith, *Energy Environ. Sci.* **2014**, *7*, 3061.
[22] M. H. Kumar, S. Dharani, W. L. Leong, P. P. Boix, R. R. Prabhakar, T. Baikie, C. Shi, H. Ding, R. Ramesh, M. Asta, M. Graetzel, S. G. Mhaisalkar, N. Mathews, *Adv. Mater.* **2014**, *26*, 7122.
[23] T.-B. Song, T. Yokoyama, S. Aramaki, M. G. Kanatzidis, *ACS Energy Lett.* **2017**, *2*, 897.
[24] K. P. Marshall, R. I. Walton, R. A. Hatton, *J. Mater. Chem. A Mater.* **2015**, *3*, 11631.
[25] H. Wang, H. Liu, Q. Zhao, C. Cheng, W. Hu, Y. Liu, *Adv. Mater.* **2016**, *28*, 624.
[26] U. Mandadapu, B. J. Babu, *Int. J. Renewable Energy Res.* **2017**, *7*.
[27] L.-Y. Huang, W. R. L. Lambrecht, *Phys. Rev. B: Condens. Matter. Mater. Phys.* **2013**, *88*, 165203.
[28] I. Chung, B. Lee, J. He, R. P. H. Chang, M. G. Kanatzidis, *Nature* **2012** *485*, 486.
[29] C. H. Ng, K. Nishimura, N. Ito, K. Hamada, D. Hirotani, Z. Wang, F. Yang, S. Likubo, Q. Shen, K. Yoshino, T. Minemoto, S. Hayase, *Nano Energy* **2019**, *58*, 130.
[30] M. Chen, M.-G. Ju, H. F. Garces, A. D. Carl, L. K. Ono, Z. Hawash, Y. Zhang, T. Shen, Y. Qi, R. L. Grimm, D. Pacifici, X. C. Zeng, Y. Zhou, N. P. Padture, *Nat. Commun.* **2019**, *10*, 16.
[31] M. Liu, H. Pasanen, H. Ali-Löytty, A. Hiltunen, K. Lahtonen, S. Qudsia, J.-H. Smått, M. Valden, N. V. Tkachenko, P. Vivo, *Angew. Chem., Int. Ed.* **2020**, *59*, 22117.
[32] N. Ito, M. A. Kamarudin, D. Hirotani, Y. Zhang, Q. Shen, Y. Ogomi, S. Iikubo, T. Minemoto, K. Yoshino, S. Hayase, *J. Phys. Chem. Lett.* **2018**, *9*, 1682.
[33] E. Jokar, C.-H. Chien, C.-M. Tsai, A. Fathi, E. W.-G. Diau, *Adv. Mater.* **2019**, *31*, 1804835.
[34] S. Shao, J. Dong, H. Duim, G. H. Ten Brink, G. R. Blake, G. Portale, M. A. Loi, *Nano Energy* **2019**, *60*, 810.
[35] K. Nishimura, M. A. Kamarudin, D. Hirotani, K. Hamada, Q. Shen, S. Iikubo, T. Minemoto, K. Yoshino, S. Hayase, *Nano Energy* **2020**, *74*, 104858.
[36] X. Jiang, F. Wang, Q. Wei, H. Li, Y. Shang, W. Zhou, C. Wang, P. Cheng, Q. Chen, L. Chen, Z. Ning, *Nat. Commun.* **2020**, *11*, 1245.
[37] T. Nakamura, S. Yakumaru, M. A. Truong, K. Kim, J. Liu, S. Hu, K. Otsuka, R. Hashimoto, R. Murdey, T. Sasamori, H. D. Kim, H. Ohkita, T. Handa, Y. Kanemitsu, A. Wakamiya, *Nat. Commun.* **2020**, *11*, 3008.
[38] C. Wang, F. Gu, Z. Zhao, H. Rao, Y. Qiu, Z. Cai, G. Zhan, X. Li, B. Sun, X. Yu, B. Zhao, Z. Liu, Z. Bian, C. Huang, *Adv. Mater.* **2020**, *32*, 1907623.
[39] M. A. Kamarudin, D. Hirotani, Z. Wang, K. Hamada, K. Nishimura, Q. Shen, T. Toyoda, S. Iikubo, T. Minemoto, K. Yoshino, S. Hayase, *J. Phys. Chem. Lett.* **2019**, *10*, 5277.
[40] M. Chen, M.-G. Ju, M. Hu, Z. Dai, Y. Hu, Y. Rong, H. Han, X. C. Zeng, Y. Zhou, N. P. Padture, *ACS Energy Lett.* **2019**, *4*, 276.
[41] J. Qiu, Y. Xia, Y. Zheng, W. Hui, H. Gu, W. Yuan, H. Yu, L. Chao, T. Niu, Y. Yang, X. Gao, Y. Chen, W. Huang, *ACS Energy Lett.* **2019**, *4*, 1513.
[42] B.-B. Yu, Z. Chen, Y. Zhu, Y. Wang, B. Han, G. Chen, X. Zhang, Z. Du, Z. He, *Adv. Mater.* **2021**, *33*, 2102055.
[43] C. Wang, Y. Zhang, F. Gu, Z. Zhao, H. Li, H. Jiang, Z. Bian, Z. Liu, *Matter* **2021**, *4*, 709.
[44] X. Liu, T. Wu, J-Y. Chen, X. Meng, X. He, T. Noda, H. Chen, X. Yang, H. Segawa, Y. Wang, L. Han. *Energy Environ. Sci.* **2020**, *13*, 2896.
[45] X. Liu, Y. Wang, T. Wu, X. He, X. Meng, J. Barbaud, H. Chen, H. Segawa, X. Yang, L. Han, *Nat. Commun.* **2020**, *11*, 2678.
[46] X. Meng, Y. Wang, J. Lin, X. Liu, X. He, J. Barbaud, T. Wu, T. Noda, X. Yang, L. Han, *Joule* **2020**, *4*, 902.

[47] I. Vázquez-Fernández, S. Mariotti, O. S. Hutter, M. Birkett, T. D. Veal, T. D. C. Hobson, L. J. Phillips, L. Danos, P. K. Nayak, H. J. Snaith, W. Xie, M. P. Sherburne, M. Asta, K. Durose, *Chem. Mater.* **2020**, *32*, 6676.
[48] D. Schwartz, R. Murshed, H. Larson, B. Usprung, S. Soltanmohamad, R. Pandey, E. S. Barnard, A. Rockett, T. Hartmann, I. E. Castelli, S. Bansal, *Phys. Status Solidi RRL* **2020**, *14*, 2000182.
[49] B. Schu, P. Heines, A. Savin, H.-L. Keller, *Inorg. Chem.* **2000**, *39*, 732.
[50] M. Chen, M.-G. Ju, A. D. Carl, Y. Zong, R. L. Grimm, J. Gu, X. Ch. Zeng, Y. Zhou, N. P. Padture, *Joule* **2018**, *2*, 558.
[51] K.-Z. Du, W. Meng, X. Wang, Y. Yan, D. B. Mitzi, *Angew. Chem.* **2017**, *129*, 8270.
[52] E. T. Mcclure, M. R. Ball, W. Windl, P. M. Woodward, *Chem. Mater.* **2016**, *28*, 1348.
[53] S. Ullah, J. Wang, P. Yang, L. Liu, J. Khan, S.-E. Yang, T. Xia, H. Guo, Y. Chen, *Sol. RRL* **2021**, *5*, 2000830.
[54] X. Nairui, T. Yehua, Q. Yali, L. Duoduo, W. Ke-Fan, *Sol. Energy* **2020**, *204*, 429.
[55] B. Li, Y. Zhang, L. Fu, T. Yu, S. Zhou, L. Zhang, L. Yin, *Nat. Commun.* **2018**, *9*, 1076.
[56] P. Wang, X. Zhang, Y. Zhou, Q. Jiang, Q. Ye, Z. Chu, X. Li, X. Yang, Z. Yin, J. You, *Nat. Commun.* **2018**, *9*, 2225.
[57] B. Lee, C. C. Stoumpos, N. Zhou, F. Hao, C. Malliakas, C.-Y. Yeh, T. J. Marks, M. G. Kanatzidis, R. P. H. Chang, *J. Am. Chem. Soc.* **2014**, *136*, 15379.
[58] B. Saparov, J.-P. Sun, W. Meng, Z. Xiao, H-S. Duan, O. Gunawan, D. Shin, I. G. Hill, Y. Yan, D. B. Mitzi, *Chem. Mater.* **2016**, *28*, 2315.
[59] X. Qiu, B. Cao, S. Yuan, X. Chen, Z. Qiu, Y. Jiang, Q. Ye, H. Wang, H. Zeng, J. Liu, M. G. Kanatzidis, *Sol. Energy Mater. Sol. Cells* **2017**, *159*, 227.
[60] G. Kapil, T. Ohta, T. Koyanagi, M. Vigneshwaran, Y. Zhang, Y. Ogomi, S. S. Pandey, K. Yoshino, Q. Shen, T. Toyoda, Md. M. Rahman, T. Minemoto, T. N. Murakami, H. Segawa, S. Hayase, *J. Phys. Chem. C* **2017**, *121*, 13092.
[61] S. R. Kavanagh, C. N. Savory, S. M. Liga, G. Konstantatos, A. Walsh, D. O. Scanlon, *J. Phys. Chem. Lett.* **2022**, *13*, 10965.
[62] A. E. Maughan, A. M. Ganose, M. M. Bordelon, E. M. Miller, D. O. Scanlon, J. R. Neilson, *J. Am. Chem. Soc.* **2016**, *138*, 8453.
[63] X. Qiu, Y. Jiang, H. Zhang, Z. Qiu, S. Yuan, P. Wang, B. Cao, *Phys. Status Solidi RRL* **2016**, *10*, 587.
[64] J. Zhang, S. Li, P. Yang, W. Liu, Y. Liao, *J. Mater. Sci.* **2018**, *53*, 4378.
[65] W. Zhu, T. Yao, J. Shen, W. Xu, B. Gong, Y. Wang, J. Lian, *J. Phys. Chem. C* **2019**, *123*, 9575.
[66] W. Zhu, G. Xin, Y. Wang, X. Min, T. Yao, W. Xu, M. Fang, S. Shi, J. Shi, J. Lian, *J. Mater. Chem. A Mater.* **2018**, *6*, 2577.
[67] S. Ullah, J. Wang, M. H. Alvi, R. Chang, P. Yang, L. Liu, S.-E. Yang, T. Xia, H. Guo, Y. Chen, *Int. J. Energy Res.* **2021**, *45*, 1720.
[68] S. T. Umedov, A. V. Grigorieva, L. S. Lepnev, A. V. Knotko, K. Nakabayashi, S.-I. Ohkoshi, A. V. Shevelkov, *Front. Chem.* **2020**, *8*, 564.
[69] S. T. Umedov, D. B. Khadka, M. Yanagida, A. Grigorieva, Y. Shirai, *Sol. Energy Mater. Sol. Cells*, **2021**, *230*, 111180.
[70] J. Wu, Z. Zhao, Y. Zhou, *Sci. Rep.* **2022**, *12*, 935.
[71] B. Lee, A. Krenselewski, S. I. Baik, D. N. Seidman, R. P. H. Chang, *Sustainable Energy Fuels* **2017**, *1*, 710.
[72] J. Huang, C. Dong, Y. Mei, X. Lu, G. Yue, Y. Gao, R. Liu, W. Zhang, F. Tan, *J. Mater. Chem. C Mater.* **2021**, *9*, 14217.
[73] F. Guo, Z. Lu, D. Mohanty, T. Wang, I. B. Bhat, S. Zhang, S. Shi, M. A. Washington, G.-C. Wang, T.-M. Lu, *Mater. Res. Lett.* **2017**, *5*, 540.
[74] B. Lee, B. Shin, B. Park, *Electron. Mater. Lett.* **2019**, *15*, 192.
[75] C. Walkons, R. Murshed, S. Bansal, *Sol. RRL* **2020**, *4*, 2000299.
[76] N. De Marco, H. Zhou, Q. Chen, P. Sun, Z. Liu, L. Meng, E.-P. Yao, Y. Liu, A. Schiffer, Y. Yang, *Nano Lett.* **2016**, *16*, 1009.
[77] N. D. Pham, V. T. Tiong, D. Yao, W. Martens, A. Guerrero, J. Bisquert, H. Wang, *Nano Energy* **2017**, *41*, 476.
[78] N. D. Pham, C. Zhang, V. T. Tiong, S. Zhang, G. Will, A. Bou, J. Bisquert, P. E. Shaw, A. Du, G. J. Wilson, H. Wang, *Adv. Funct. Mater.* **2019**, *29*, 1806479.
[79] J. Tong, Z. Song, D. H. Kim, X. Chen, C. Chen, A. F. Palmstrom, P. F. Ndione, M. O. Reese, S. P. Dunfield, O. G. Reid, J. Liu, F. Zhang, S. P. Harvey, Z. Li, S. T. Christensen, G. Teeter, D. Zhao, M. M. Al-Jassim, M. F. A. M. Van Hest, M. C. Beard, S. E. Shaheen, J. J. Berry, Y. Yan, K. Zhu, *Science* **2019**, *364*, 475.
[80] J. Zou, W. Liu, W. Deng, G. Lei, S. Zeng, J. Xiong, H. Gu, Z. Hu, X. Wang, J. Li, *Electrochim. Acta* **2018**, *291*, 297.
[81] M.-S. Lee, S. Sarwar, S. Park, U. Asmat, D. T. Thuy, C.-H. Han, S. J. Ahn, I. Jeong, S. Hong, *Sustainable Energy Fuels* **2020**, *4*, 3318.
[82] S. J. Lee, S. S. Shin, Y. C. Kim, D. Kim, T. K. Ahn, J. H. Noh, J. Seo, S. I. Seok, *J. Am. Chem. Soc.* **2016**, *138*, 3974.
[83] E. Gu, X. Tang, S. Langner, P. Duchstein, Y. Zhao, I. Levchuk, V. Kalancha, T. Stubhan, J. Hauch, H. J. Egelhaaf, D. Zahn, A. Osvet, C. J. Brabec, *Joule* **2020**, *4*, 1806.
[84] F. Hao, C. C. Stoumpos, P. Guo, N. Zhou, T. J. Marks, R. P. H. Chang, M. G. Kanatzidis, *J. Am. Chem. Soc.* **2015**, *137*, 11445.
[85] J. Pascual, D. D. Girolamo, M. A. Flatken, M. H. Aldamasy, G. Li, M. Li, A. Abate, *Eur. J.* **2022**, *28*, e202103919.
[86] A. Singh, M. K. Jana, D. B. Mitzi, *Adv. Mater.* **2021**, *33*, 2005868.
[87] Z. Zhang, M. A. Kamarudin, A. K. Baranwal, G. Kapil, S. R. Sahamir, Y. Sanehira, M. Chen, L. Wang, Q. Shen, S. Hayase, *Agnew. Chem., Int. Ed.* **2022**, *61*, e202210101.
[88] M. Taddei, J. A. Smith, B. M. Gallant, S. Zhou, R. J. E. Westbrook, Y. Shi, J. Wang, J. N. Drysdale, D. P. Mccarthy, S. Barlow, S. R. Marder, H. J. Snaith, D. S. Ginger, *ACS Energy Lett.* **2022**, *7*, 4265.
[89] T.-B. Song, T. Yokoyama, J. Logsdon, M. R. Wasielewski, S. Aramaki, M. G. Kanatzidis, *ACS Appl. Energy Mater.* **2018**, *1*, 4221.
[90] E. Jokar, C.-H. Chien, A. Fathi, M. Rameez, Y.-H. Chang, E. W.-G. Diau, *Energy Environ. Sci.* **2018** *11*, 2353.
[91] L. H. Chi, T. T. D. Lien, N. T. Dai, N. T. Thanh, P. Van Phuc, N. T. T. Oanh, P. D. Long, P. Van Hoi, *Mater. Res. Express* **2019**, *6*, 116442.
[92] A. G. Kontos, A. Kaltzoglou, E. Siranidi, D. Palles, G. K. Angeli, M. K. Arfanis, V. Psycharis, Y. S. Raptis, E. I. Kamitsos, P. N. Trikalitis, C. C. Stoumpos, M. G. Kanatzidis, P. Falaras, *Inorg. Chem.* **2017**, *56*, 84.
[93] J.-S. Yeo, R. Kang, S. Lee, Y.-J. Jeon, N. S. Myoung, C.-L. Lee, D.-Y. Kim, J.-M. Yun, Y.-H. Seo, S.-S. Kim, S.-I. Na, *Nano Energy* **2015**, *12*, 96.
[94] https://www.silitech.ch/wp-content/uploads/fiche_technique_f/466.pdf (accessed: October 2022).